PAPER

Check for updates

Eco-friendly green synthesis of Fe-doped WS₂ using neem leaf extract: unlocking large interlayer spacing for improved capacitance and rapid ion transport

M. I. Khan,[a] Ali Mujtaba, [ID] *[a] M. Arslan Nadeem,[a] Amira Majeed,[a] Safa Ezzine[b] and Dhafer O. Alshahrani [ID] [c]

Iron-doped tungsten disulfide (Fe-WS$_2$) nanoparticles were synthesized *via* a green method using neem leaf extract. X-ray diffraction (XRD) confirmed structural changes, with the formation of a hexagonal structure. The *d*-spacing is increased by Fe doping (6.05–6.08 Å). Fourier-transform infrared (FTIR) spectroscopy identified W–S and S–S bond vibrations, crucial for material integrity. The Brunauer–Emmett–Teller (BET) analysis confirmed the increased surface area and pore radius as a result of enhanced ions diffusion. The morphology study through Scanning Electron Microscopy (SEM) revealed enhanced porosity of Fe-WS$_2$, as evidenced by the more granular and disordered structure. UV-vis spectroscopy (UV-vis) showed a blue shift and an increased energy band gap from 2.48 eV to 2.64 eV, indicating improved optical properties. Methyl blue (MB) dye adsorption spectra showed that the Fe-WS$_2$ is porous, and as a result, more electrolyte adsorbs within the electrode. Cyclic voltammetry (CV) and galvanostatic charge–discharge (GCD) revealed enhanced specific capacitance and energy density. Electrochemical impedance spectroscopy (EIS) demonstrated a significant reduction in charge transfer resistance and a substantial increase in the ion diffusion coefficient. These findings underscore the potential of Fe-WS$_2$ for high-performance energy storage devices.

1. Introduction

Among the electrochemical energy storage devices, super-capacitors have gained much attention due to their excellent power density, rapid charge–discharge rate, and long cycle life.[1] Generally, pseudocapacitors exhibit higher performance than double-layer capacitors based on the charge-storage mechanism, and the structure of electrode material plays a crucial role in energy storage. In recent years, transition metal sulfides (TMS) have been reported as emerging electrode materials for supercapacitor applications due to their excellent electroactive abilities. Various TMS such as CoS_x, Ni_3S_2, WS_2 and CuS have been used as electroactive materials for supercapacitor applications.[2,3] Among them, WS_2 nanoparticles offer several advantages that make them highly suitable for supercapacitor applications. One key advantage of WS_2 nanoparticles is their ability to improve the tribological properties of coatings, enhancing hardness, wear resistance, and reducing friction.

WS_2 is crucial for ensuring the durability and longevity of supercapacitor electrodes, especially in high-performance applications where wear and friction need to be minimized to maintain efficiency. These nanoparticles exhibit excellent mechanical strength due to their compact size and demonstrate stability at high temperatures and pressures. Moreover, WS_2 nanoparticles enhance the energy storage properties of super-capacitors.[4] By leveraging of WS_2 nanoparticles, researchers can enhance the energy density, power density, and cycling stability of supercapacitors, making them more efficient and reliable for various applications.

Wu *et al.* prepared WS_2/CoS_2 heterojunction on carbon cloth and revealed their superior HER activity at all pH.[5] Veronika *et al.*, studied the effects of doping on WS_2 and MoS_2 both in theoretically and experimentally and showed that doping significantly improved their hydrogen evolution reactivity.[6] Zhang *et al.*, used Cr as a dopant in CoP to adjust its electronic structure, and used DFT calculations to show that Cr doping reduces Gibbs free energy as the mechanism to promote HER.[7] Although WS_2 has very good electrochemical properties but there are some limitations to use WS_2 in supercapacitor applications due to their relatively low electrical conductivity, which hampers efficient charge transfer.[5,6] Although they possess a layered structure, their surface area is often less than that of

[a]Department of Physics, The University of Lahore, 53700, Pakistan. E-mail: alimujtabaaslam@gmail.com

[b]Department of Chemistry, College of Science, King Khalid University, P.O. Box 9004, 61413 Abha, Saudi Arabia

[c]Department of Physics, College of Science, University of Bisha, P.O. Box 551, Bisha 61922, Saudi Arabia

other nanomaterials, limiting their capacitance. Additionally, WS_2 can experience structural instability during repeated charge–discharge cycles, leading to performance degradation over time.[7] Furthermore, these nanoparticles tend to aggregate, reducing their effective surface area and accessibility for ions. To address these issues, doping WS_2 with transition metals enhances its properties for supercapacitors by improving electrical conductivity and increasing surface area, thereby boosting charge transfer efficiency and capacitance.[8] The doped materials exhibit better structural stability, reducing performance degradation during charge–discharge cycles.[9] Transition metal doping can also mitigate nanoparticle aggregation, ensuring greater ion accessibility. This modification ultimately leads to superior electrochemical performance and longevity in supercapacitor applications.[10] A Ni-doped WS_2 electrode was created by Keshab *et al.* using the hydrothermal approach, yielding a capacitance of 144 F g^{-1} at a current density of 1 A g^{-1}.[11] Visakh *et al.* similarly manufactured a Ni-doped WS_2 electrode, reporting an enhanced capacitance of 204 F g^{-1} at 1 A g^{-1}.[12] By employing Ru doping to accomplish 2H/1T phase coupling in WS_2 with Na_2SO_4 as the electrolyte, Pamula *et al.* were able to discover an impressive capacitance of 664 F g^{-1} at 1 A g^{-1}.[13] Using hydrothermal synthesis, Milan *et al.* concentrated on Mn-doped WS_2 microcones and reported a capacitance of 107.79 F g^{-1} at 1 A g^{-1}.[14]

Iron (Fe) atoms intercalate inside the van der Waals gaps, increasing *d*-spacing and slightly warping the WS_2 lattice.[15] By upsetting the normal stacking order, this intercalation improves ion transport pathways and promotes charge transfer. The electrolyte ions intercalate and de-intercalate between the electrode layers more rapidly as a result of higher *d*-spacing.[16] Fe increases pore radius and surface area, introducing more active sites and improving charge storage capacity. Fe doping and improved electrochemical performance are directly related, as seen by these structural modifications that increase capacitance, energy density, and charge/discharge rates.[17]

In this study, we reported the Fe doping influence on WS_2 nanoparticles prepared by green synthesis *via* neem leaf extract. Biomolecules like polyphenols and flavonoids are essential for lowering iron ions and stabilizing the resulting nanoparticles in the green synthesis method that uses neem leaf extract. While flavonoids help by forming stabilizing layers surrounding the nanoparticles, avoiding agglomeration, and guaranteeing uniform size distribution, polyphenols aid in the conversion of Fe ions to zero-valent iron through redox processes. In addition to improving the stability of the nanoparticles, this process stimulates their electrochemical activity, including capacitance and ion diffusion, which improves energy storage device performance metrics.[18,19] The Fe doping introduces more active sites and increases the interlayer layer spacing of WS_2, as a result, more ions can intercalate\de-intercalate and performance of supercapacitor will increase (Fig. 1). Electrochemical properties such as capacitance (C_{sp}), energy density (E_d), power density (P_d), charge transfer resistance (R_{ct}), and ion diffusion coefficient (D_{K^+}) of iron (Fe)-doped tungsten disulfide (WS_2) sample will be improved. Techniques such as XRD, FTIR, BET, SEM, UV-v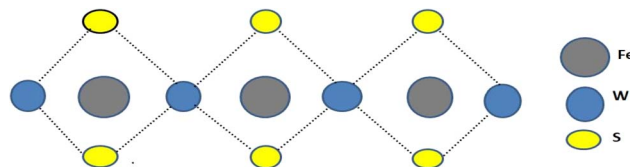is spectroscopy, CV, GCD, and EIS were employed to analyze the samples. This study provides a comprehensive analysis of the effects of Fe doping on WS_2, highlighting its potential for applications in energy storage devices such as supercapacitors.

Fig. 1 Structure of Fe-WS_2 material.

2. Experimental details

Fe-doped WS_2 was prepared by the green synthesis method. The green synthesis of 10% Fe-doped WS_2 using *Azadirachta indica* (neem) leaf extract is employed due to its eco-friendly nature, cost-effectiveness, and simplicity. Neem leaves contain natural reducing agents and stabilizers like polyphenols, flavonoids, and terpenoids, which facilitate the reduction of metal ions and stabilize the nanoparticles. The presence of these biomolecules aids in forming uniformly dispersed Fe-WS_2 nanoparticles with enhanced surface area and porosity. This improved morphology results in superior electrochemical properties, such as increased conductivity, better charge storage capacity, and enhanced ion diffusion. Consequently, the green synthesis method not only minimizes environmental impact but also significantly boosts the electrochemical performance of Fe-WS_2 nanoparticles.[19,20]

Firstly 9.896 g sodium tungstate ($Na_2WO_4 \cdot 2H_2O$), thiourea (CH_4N_2S) 2.283 g, and iron nitrate hexahydrate ($Fe(NO_3)_2 \cdot 9H_2O$) 1.212 g, were dispersed into 60 mL neem leaves extract solution at 0.5 M concentration and stirred for 30 min. The mixture was transferred into a 100 mL Teflon-lined autoclave, and kept at 120 °C for 8 hours. After the autoclave was cooled down to room temperature, the samples were washed thoroughly with DIW. The sample was centrifuged at 5000 rpm for 2–3 times, the final sample was dried at 70 °C for 48 hours in the oven. The product obtained was used as such for further analysis and characterized to confirm the composite formation. The XRD data of the sample was taken using a Rigaku D/MaxIIIC diffract meter with CuK_α radiation at room temperature. The optical properties of the samples were measured by UV-vis spectra LX211DS. To check the porous nature of both samples, UV-vis spectra are obtained by dissolving the material in 0.2 mg Methyl Blue (MB) with 10 mL distilled water. FTIR spectra were obtained by spectrometer 7800A.

Electrodes for supercapacitors were prepared by slurry on Ni foam. Firstly slurry was prepared by 80% material mixed with 10% activated carbon and 10% binder and stirred for 4 hours. Spread the slurry onto the Ni foil using a doctor's blade. Place the coated foil in an oven at about 50 °C for up to 16 hours (Fig. 2). Electrochemical characterization such as CV, GCD, and EIS were performed by the electrochemical system (CS350M).
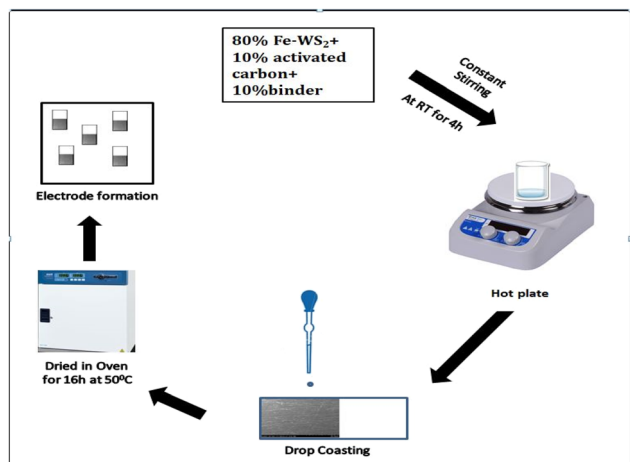
Fig. 2 Stepwise formation of the electrode.

3. Results and discussion

3.1. Structural properties

The crystal structures and phases of the as-synthesized WS_2 and Fe-WS_2 samples were determined by XRD analysis depicted in Fig. 3(a), revealing distinct diffraction peaks corresponding to specific crystal planes. The pure WS_2 sample exhibits diffraction peaks at 2θ values 14.56°, 28.89°, 32.91°, 33.79°, 35.56°, 39.89°, 43.63°, 49.79°, 35.56°, 58.47°, 58.52° and 60.86° respectively at the corresponding planes (002), (004), (100), (100), (101), (103), (006), (102), (105), (110), (008), and (112) respectively crystal planes of the hexagonal WS_2 structure, according to PDF# 37-1942.[21,22] The peaks intensities in the Fe-WS_2 sample are reduced and new peaks of FeS are produced at planes 31.15° (100), 47.71° (102), and 56.68° (110) due to Fe interaction with 'S' (PDF card no. 65-5762).[23] It might be possible that during the synthesis process of thiourea, $(Fe(NO_3)_2 \cdot 9H_2O)$, $Na_2WO_4 \cdot 2H_2O$, some Fe ions might react with 'S' in thiourea due to the large amount of Fe. Therefore, the FeS new compound has been formed.[23] The reduced crystallinity and formation of FeS can enhance electrochemical properties, as the disturbed structure increases active sites and conductivity, making Fe-WS_2 beneficial for supercapacitors by improving charge storage and cycling stability.[24] The Fe-WS_2 samples reveal slight shifts in the peak towards smaller angles, at the plane (002) due to the larger ionic radius of Fe^{2+} (0.76 Å) compared to W^{6+} (0.60 Å),[24] which showed the increase in interlayer spacing, according to Bragg's Law. The calculated d-spacing at the highest peak (002) increased from 6.05 Å to 6.08 Å. The intercalated Fe ions may be produced electrostatic repulsion due to which the d-spacing is increased. Increased d-spacing from Fe doping improves supercapacitors by enhancing the surface area for charge storage, facilitating faster ion intercalation\de-intercalation, as a result, performance of the capacitor is enhanced.[25]

The crystallite size (D) and the microstrain (ε) is computed using the following Williamson–Hall (W–H) relation:[26]

$$\beta = \frac{0.9\lambda}{D\cos\theta} + 4\varepsilon\tan\theta \quad (1)$$

The wavelength and FWHM were denoted by λ (1.542 Å) and β, respectively, in eqn (2). The micro-strain and average crystallite size values were calculated using the slope and intercept of $\beta\cos\theta$ vs. $\sin\theta$ plots, as shown in Fig. 3(b). The pure sample's crystallite size, as determined by the W–H plot, is 27.2 nm. This crystallite size, however, shrank to 23.9 nm in the Fe-doped sample. These results imply that the addition of Fe doping encourages grain contraction, which results in the development of shorter crystallites.[26,33] Additionally, the pure sample's microstrain (ε) is 4.6×10^{-3}, while the Fe-doped sample is -3.10×10^{-3}. While the Fe-doped sample has a negative value indicating compressive strain, the pure sample has a positive microstrain value showing tensile strain.[26] These variations, which are brought on by differences in the ionic radii between Fe and W, lead to lower compressive strain.[27]

The dislocation line density (δ), and d-spacing (d), are observed by the given formulas:[28]

$$\delta = \frac{1}{D^2} \quad (2)$$

$$d = \frac{n\lambda}{2\sin\theta} \quad (3)$$

Here β, θ, λ and n, are FWHM, Bragg's angle, wavelength, and diffraction order. Dislocation line density (ρ) is the measure of the total length of dislocation lines per unit volume in a crystalline material. The calculated DLD increase from 1.35×10^{-12} to 1.75×10^{-12} m^{-2} (Table 1). Fe doping in WS_2 introduces lattice strain due to the size and valence mismatch between Fe and W atoms, creating localized distortions.[29] This strain energy promotes dislocation formation as the crystal structure minimizes distortion.[30] The increased dislocation density impedes grain boundary movement, hindering grain growth and resulting in smaller grains.[31] This process is energetically favorable as it reduces overall strain energy. Consequently, the material exhibits enhanced hardness and strength due to the higher dislocation density and smaller crystallite size.[32] The strain (ε) and stress (σ) are calculated by given formulas:[33,34]

$$\varepsilon = \frac{\beta\cos\theta}{4} \quad (4)$$

$$\sigma = C\varepsilon \quad (5)$$

In above expression, bulk Young's modulus (1.46 ± 10^{10} N m^{-2}) is denoted by the letter "C". The calculated strain values for the pure WS_2 and Fe-WS_2 increased from 5.21×10^{-4} to 8.93×10^{-4} and stress increased from 7.60×10^6 N m^{-2} to 1.30×10^7 N m^{-2}. The increase in strain and stress occurs because Fe atoms, having a larger atomic radius than W atoms, create a size mismatch when incorporated into the WS_2 lattice.[35] This size difference causes local distortions in the lattice structure, as the lattice must expand to fit the larger Fe atoms. These distortions introduce additional internal stresses as the surrounding lattice adjusts, leading to increased strain within the material.[36] Increased strain from Fe doping can enhance pseudo capacitance by creating more active sites for charge storage and
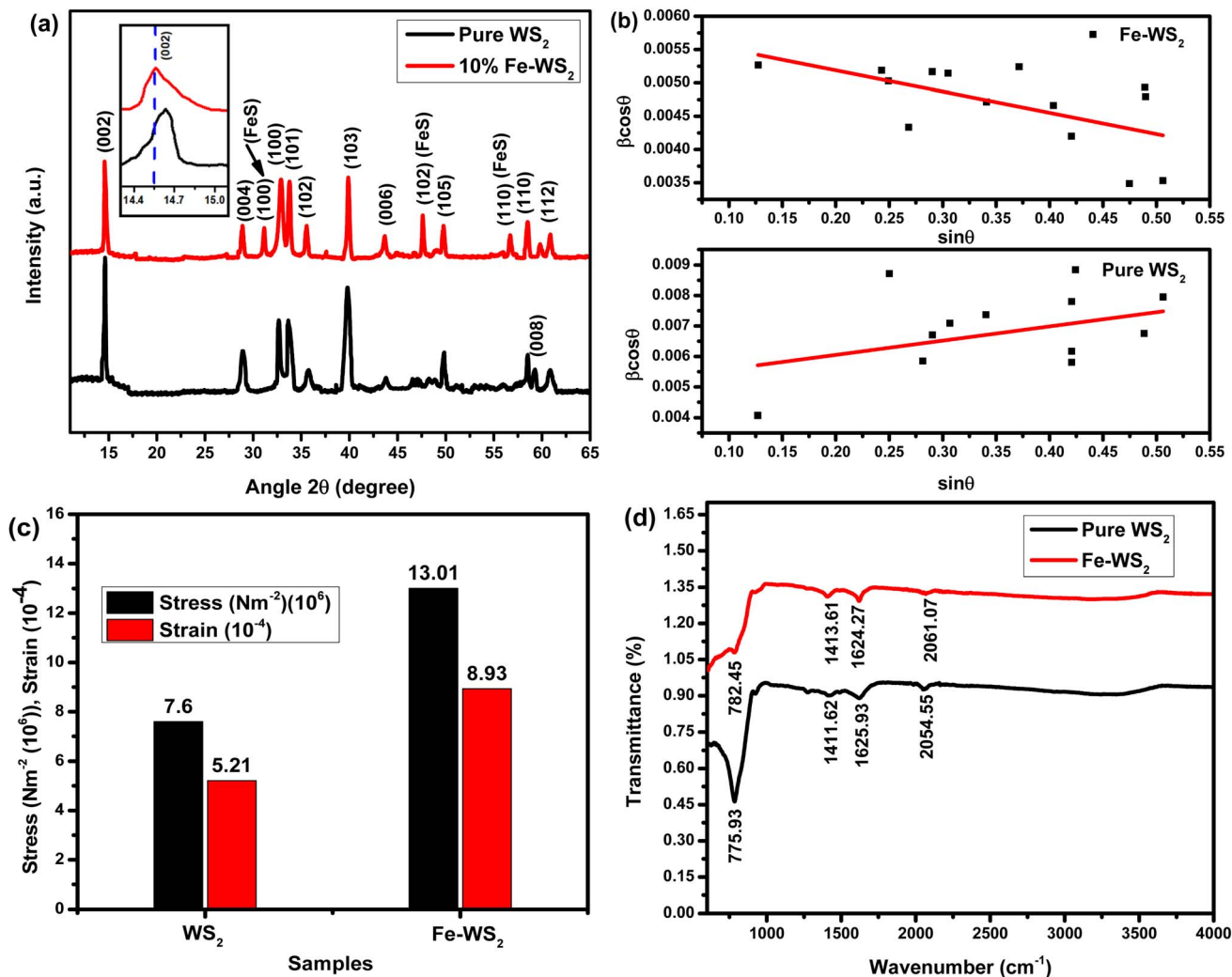
Fig. 3 (a) XRD pattern, (b) relation between grain size, dislocation line density and d-spacing, (c) relation between stress and strain, (d) FTIR graph of pure WS$_2$ and Fe-WS$_2$.

Table 1   XRD calculated parameters of WS$_2$ and Fe-WS$_2$

Parameter	Pure WS$_2$	Fe-WS$_2$
Crystallite size (nm)	27.2	23.9
Dislocation density (m^{-2})	1.35×10^{-12}	1.75×10^{-12}
d-spacing (Å)	6.050	6.079
Strain (ε)	5.21×10^{-4}	8.93×10^{-4}
Stress (σ) (Pa)	7.60×10^{6}	1.30×10^{7}

enhance the process of electrolyte ions intercalation\de-intercalation.[37]

FTIR characterization confirms the successful synthesis and bonding environments within WS$_2$ and Fe-doped WS$_2$ nano-structures (Fig. 3(d)). The FTIR spectrum of pure tungsten disulfide (WS$_2$) shows peaks at 775.93 cm^{-1} and 1411.85 cm^{-1}, which correspond to specific vibrational movements of the atoms within the material. The peak at 1625.93 cm^{-1} is attributed to the stretching vibrations of tungsten–sulfur (W–S) bonds, while the peak at 2054.55 cm^{-1} is associated with sulfur–sulfur

(S–S) bond stretching. In the case of 10% Fe-doped WS$_2$, the FTIR spectrum displays peaks at 782.45 cm^{-1}, 1413.61 cm^{-1}, 1625.27 cm^{-1}, and 2061.07 cm^{-1}. These peaks correspond to similar vibrational movements as in pure WS$_2$ but exhibit slight shifts due to the incorporation of iron.[38] The shifts in the W–S and S–S stretching vibration peaks suggest that Fe doping has caused changes in the lattice structure and bonding environment of the WS$_2$, which in turn affects its vibrational properties.[39,40] In the synthesis of Fe-WS$_2$, biomolecules in neem leaf extract act as natural reducing and stabilizing agents, enabling the incorporation of Fe ions into the WS$_2$ structure.[41] Although no new peaks appear in the FTIR spectra of Fe-WS$_2$, a reduction in peak intensity at 782, 1413, 1624, and 2061 cm^{-1} is observed compared to pure WS$_2$, suggesting interaction between Fe ions and the biomolecules.[42] This decrease in intensity indicates effective capping and stabilization by biomolecules, confirming their role in the Fe doping process.[43]

Using nitrogen adsorption–desorption isotherms, the Brunauer–Emmett–Teller (BET) approach was used to determine
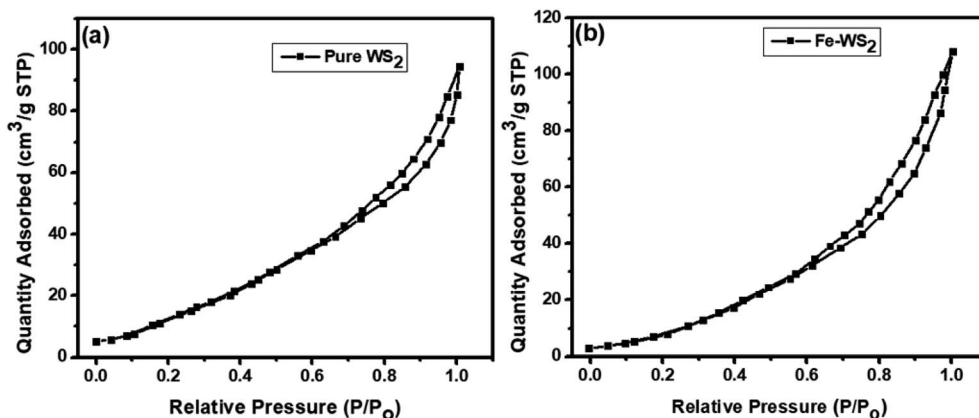
Paper

RSC Advances

Fig. 4 BET analysis (a) pure WS_2 (b) Fe-doped WS_2 nanostructures.

the pore size and specific surface area of the pure and Fe-doped WS_2 materials (Fig. 4). According to the IUPAC classification, the BET analysis of both materials shows Type-IV isotherms, supporting the surface's mesoporous nature.[44] An average pore radius of 10.31 nm and a surface area of 73.35 m^2 g^{-1} is found for pure WS_2, whereas an average pore radius of 31.47 nm and a surface area of 104.16 m^2 g^{-1} is found for the Fe-doped sample. When compared to pure WS_2, the BET analysis shows that the Fe-doped WS_2 has a larger pore size. Nonetheless, the Fe-doped samples with a greater region of hysteresis loop show an improved pore size distribution.[45] As a result, the produced

Fe-doped sample has a porous structure and larger pore size, both of which are essential for an effective electrochemical application.[45]

3.2. Morphological analysis

The SEM images in Fig. 5(a)–(d) show how Fe doping affects the morphology of WS_2. In Fig. 5(a), pure WS_2 appears more crystalline with larger grain sizes, indicating well-formed crystallites. In Fig. 5(b), Fe-doped WS_2 shows a more granular and disordered structure, which suggests a decrease in crystal size.
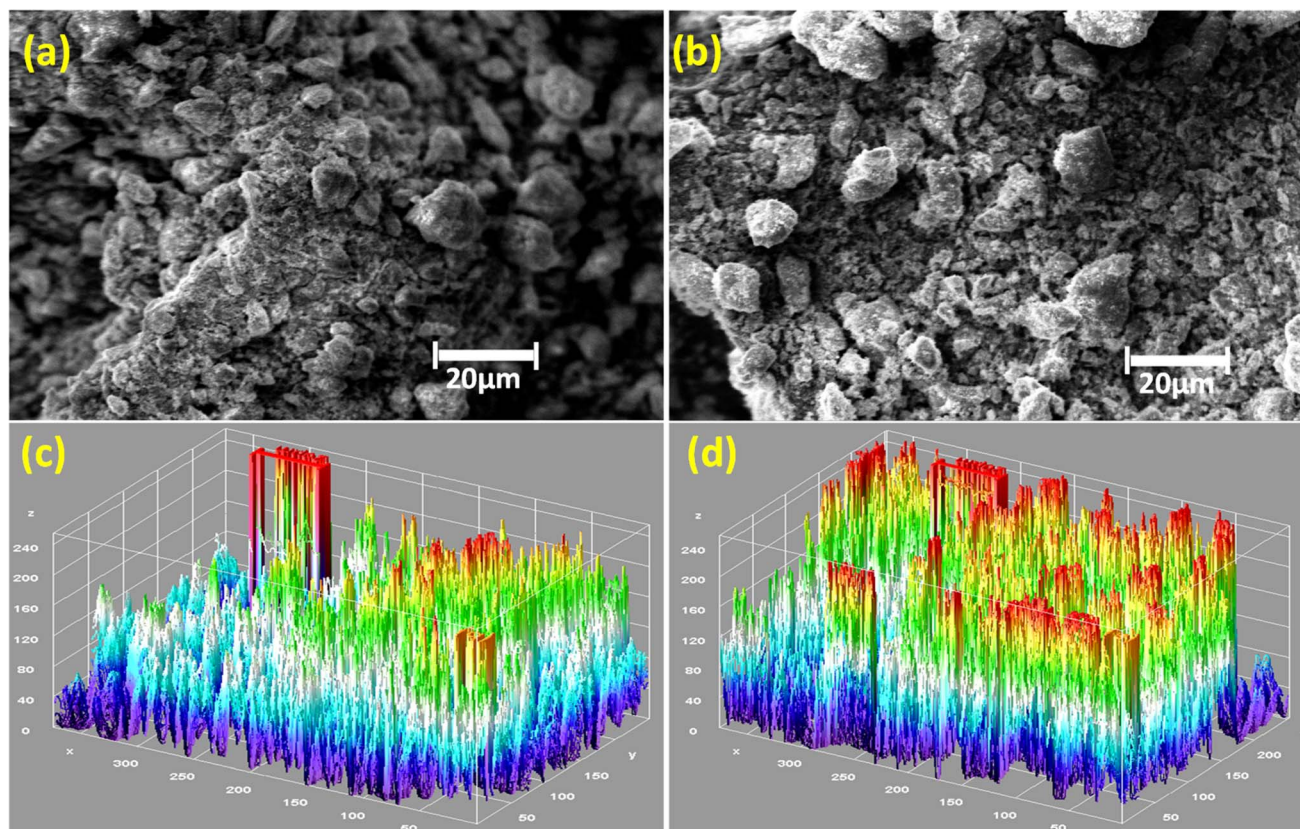

Fig. 5 (a) SEM image of pure WS_2 (b) SEM image of Fe-WS_2 (c) 3D image of pure WS_2 (d) 3D image of Fe-WS_2.

This aligns with XRD results, where Fe doping typically leads to broader peaks, indicating smaller crystallite sizes.[28,46] The granular and disordered structure of the Fe-doped sample enhanced porosity observed in the SEM image. In Fig. 5(c) and (d), the 3D SEM images provide further insight into the surface topography. Fig. 4(c) shows the 3D surface of pure WS_2, which appears less rugged and has fewer peaks and valleys, consistent with lower porosity.[38] On the other hand, Fig. 5(d) reveals the 3D surface of Fe-WS_2, characterized by a highly uneven, rough structure with a greater number of voids and pores. This increased porosity upon Fe doping is crucial for enhancing the performance of supercapacitors. The porous structure allows for better accessibility and distribution of electrolyte ions within the material, facilitating faster ion diffusion and greater surface area for charge storage. This ultimately contributes to improved electrochemical performance in supercapacitor applications, where high surface area and efficient ion transport are critical.[38]

3.3. Optical properties

The UV-vis spectroscopy analysis of WS_2 and Fe-WS_2 reveals significant insights into their optical properties and electronic structures, as shown in Fig. 6(a). The maximum absorbance for WS_2 is observed at a wavelength of 438 nm, while for Fe-WS_2 it shifts to 430 nm, indicating a blue shift due to Fe doping. The blue shift in the UV-vis absorption spectrum indicates that Fe doping in WS_2 alters the electrical structure and increases the band gap. The interactions between the Fe (3d) and W (5d) orbitals are responsible for this shift. The band structure is essentially changed by the localized states that the Fe (3d) orbital states introduce close to the conduction band edge.[47] Moreover, according to the quantum confinement concept, the decreases in the crystallite size lead to an increase in the energy band gap.[48] The observed blue shift is caused by both quantum confinement and the electronic interaction between the Fe and W subshells, which validates the influence of Fe doping on
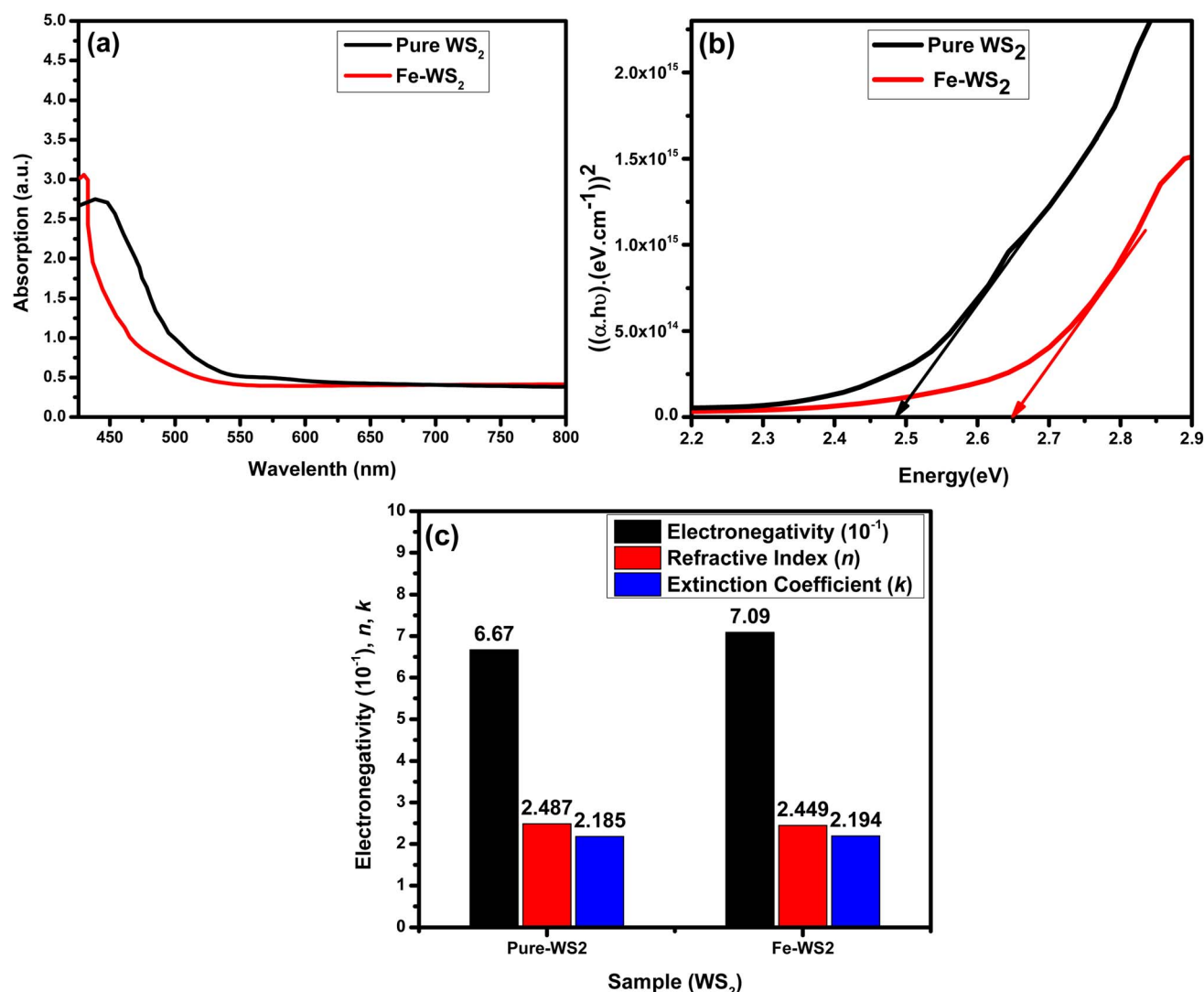

Fig. 6 (a) UV absorption graph, (b) Tau'c graph, (c) graph between electronegativity refractive index and extinction coefficient of pure WS_2 and Fe-WS_2.

the optical characteristics of WS_2.[49,50] The band gap energy (E_g)) was determined using the Tau'c equation.[51]

$$(\alpha h\nu)^2 = A(h\nu - E_g) \qquad (6)$$

Here α is the absorption coefficient, h is Planck's constant, ν is the frequency of the incident light, A is a constant and E_g is the band gap energy. The bandgap energy for WS_2 is found to be 2.48 eV, and for Fe-WS_2, it increases to 2.64 eV, as shown in (Fig. 6(b)). Fe doping in WS_2 increases the energy bandgap due to the introduction of Fe atoms into the lattice, which affects the electronic structure.[29] The Fe atoms create additional impurity states within the band structure, resulting in a wider bandgap which perturbation leads to an increase in the energy required for electron transitions from the valence band to the conduction band.[52] Electronegativity values for the samples were also calculated, resulting in 0.667 for WS_2 and 0.709 for Fe-WS_2. The refractive index 'n' and extinction coefficient 'k' are related to the real and imaginary parts of the dielectric constant the following equations:[53,54]

$$n = \sqrt{\left(\frac{A}{B + E_g}\right)^2 + 1} \qquad (7)$$

$$K = \frac{n}{\Delta x^{*}\gamma} \qquad (8)$$

The constants "A" and "B" for semiconductor material in the above relation have values of 13.6 and 3.4, respectively. The calculated n for pure WS_2 and doped Fe-WS_2 is 2.48 and 2.44 respectively, while the value of K for WS_2 and Fe-WS_2 are 2.185 to 2.194 respectively (Fig. 6(c)). The decrease in refractive index after Fe doping is due to changes in electronic polarizability.[55] Fe introduces defects and impurity states that disrupt the electronic distribution, reducing the material's ability to polarize in response to an electric field.[56] This leads to a lower refractive index, as the material's interaction with light is altered. The increase in the k with Fe doping arises from the

introduction of new electronic states or modifications to existing ones.[57] This enhanced absorption is linked to the changes in the electronic structure induced by Fe doping.[58,59]

The UV-vis study lies in demonstrates that Fe-doping in WS_2 introduces a blue shift in the UV-vis absorption profile, indicating an increased band gap.[60] This change enhances the material's adsorptive properties and porosity, crucial for supercapacitor performance.[60] Fig. 7 displays the UV-vis absorption spectra of pure WS_2 and Fe-doped WS_2 in MB. At 595.13 nm and 654.17 nm, the absorption peak intensity for Fe-WS_2 is significantly lower than that for pure WS_2, indicating high adsorption capacity. This large absorption suggests that Fe-WS_2 has enhanced adsorptive properties, likely due to increased porosity. The higher porosity facilitates greater electrolyte absorption, which is crucial for improving ion transport and charge storage capabilities.[61] These properties are advantageous for supercapacitors, as they can enhance the device's energy storage performance and efficiency by allowing more active sites for electrochemical reactions and improving overall conductivity.

3.4. Electrochemical properties

The WS_2 and Fe-WS_2 nanoparticles and the electrochemical behaviors propose their applications as advanced electrode materials for high-performance supercapacitors. The energy storage performance of the WS_2 electrode was also evaluated by CV, GCD, and EIS measurements with 1 M KOH in 100 mL electrolyte solution. The CV plots of the WS_2 electrode and Fe-WS_2 are shown in Fig. 8(a) and (b). The CV profiles of the Fe-WS_2 nanocomposites show an improved current response within the range of 5–50 mV s^{-1}, indicating a greater capacitance. With increasing the scan rates, the area of the CV curve is enhanced, and the anodic and cathodic peaks shift in more positive and negative directions.[62] Even at higher scan rates, CV curves show undetectable changes in the shape, indicating that the Fe-WS_2 electrode is favorable for rapid reversible redox reactions (Fig. 8(c)). The specific capacitance (C_s) (F g^{-1}) and energy density (E) (W h kg^{-1}) were determined from the CV curves by using the equations below.[63]

$$C_{sp} = \frac{A_{area}}{\nu \Delta V m} \qquad (9)$$

$$E_d = \frac{C_s \times \left(V_{max}^2 - V_{min}^2\right)}{7.2} \qquad (10)$$

As a function of current density, the C_s values of the pure WS_2 electrode from the plots were about 194.8 F g^{-1}, 105.6 F g^{-1}, 62.2 F g^{-1}, 51.5 F g^{-1}, 43.18 F g^{-1}, and 36.42 F g^{-1} at scan rate 5 mV s^{-1}, 10 mV s^{-1}, 20 mV s^{-1}, 30 mV s^{-1}, 40 mV s^{-1}, and 50 mV s^{-1} respectively (Fig. 8(c)). The specific capacitance of Fe-WS_2 at scan rate 5 mV s^{-1}, 10 mV s^{-1}, 20 mV s^{-1}, 30 mV s^{-1}, 40 mV s^{-1}, and 50 mV s^{-1} respectively is 324.7 F g^{-1}, 176.1 F g^{-1}, 103.7 F g^{-1}, 85.9 F g^{-1}, 71.9 F g^{-1}, and 60.7 F g^{-1} obtained correspondingly (Fig. 8(c)). The increase in specific capacitance with Fe doping in WS_2 is primarily due to the introduction of additional active sites and defects, which enhance charge
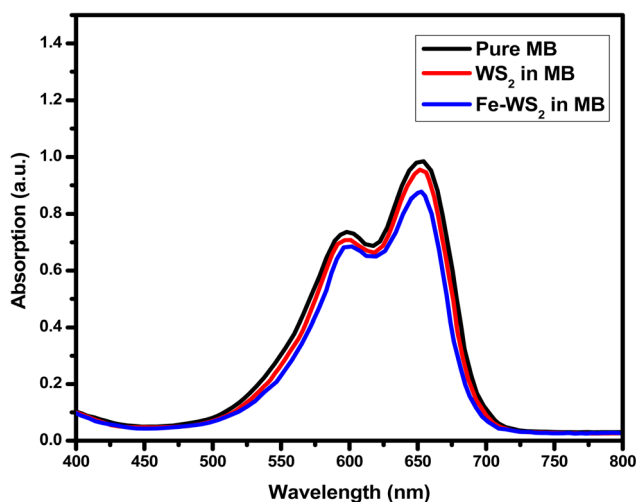

Fig. 7 UV absorption graph of pure WS_2 and Fe-doped WS_2 in MB.
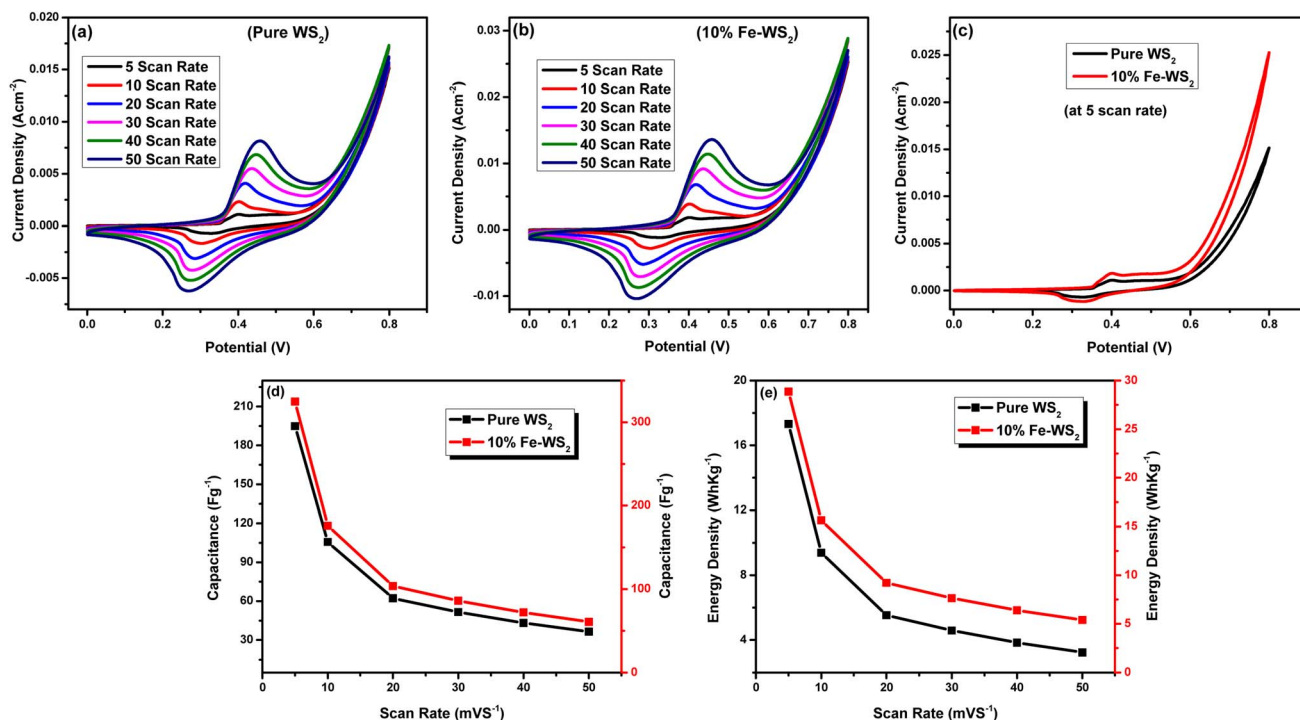
Fig. 8 (a) CV curves of pure electrode, (b) CV curves of doped electrode, (c) CV curves at 5 scan rate of both sample, (d) specific capacitance, (e) energy density of pure WS_2 and Fe-WS_2.

storage capacity.[64] The larger atomic radius of Fe compared to W causes an expansion in the lattice (increased d-spacing), allowing easier ion intercalation and faster ion diffusion. Furthermore, Fe doping improves the electronic conductivity of WS_2 by providing more pathways for charge carriers.[65] These factors collectively contribute to the increased specific capacitance observed in the CV curves. The curves suggest improved charge storage capability due to the synergy between WS_2 and Fe-WS_2. The calculated energy density values of pure WS_2 at 5 mV s^{-1}, 10 mV s^{-1}, 20 mV s^{-1}, 30 mV s^{-1}, 40 mV s^{-1}, and at 50 mV s^{-1} scan rate are 17.3 W h kg^{-1}, 9.3 W h kg^{-1}, 5.5 W h kg^{-1}, 4.4 W h kg^{-1}, 3.8 W h kg^{-1} and 3.2 W h kg^{-1} respectively. Similarly, the values of energy density of Fe-WS_2 at 5 mV s^{-1}, 10 mV s^{-1}, 20 mV s^{-1}, 30 mV s^{-1}, 40 mV s^{-1}, and at 50 mV s^{-1} scan rate is 28.8 W h kg^{-1}, 15.6 W h kg^{-1}, 9.2 W h kg^{-1}, 7.6 W h kg^{-1}, 6.3 W h kg^{-1} and 5.3 W h kg^{-1} respectively (Fig. 8(d)). The increase in energy density with Fe doping in WS_2 involves the interaction and bonding changes within the material.[66] Fe atoms, with their larger atomic radius, replace W atoms in the lattice, causing an expansion and introducing strain. This results in more active sites and defects, which enhance charge storage. The presence of Fe improves the electronic structure and conductivity of WS_2 by altering the distribution of electrons and creating more pathways for charge carriers.[67] These chemical changes collectively enhance ion intercalation, storage capacity, and overall energy density.

A GCD investigation was conducted on WS_2 electrode. The study involved varying current densities ranging from 0.8 to 2.0 A g^{-1} within a potential window of 0–0.5 V, in a 1 M KOH

solution. Fig. 9(a) and (b) displays the GCD curves of pure WS_2 and Fe-WS_2 samples respectively. The formulas below were used to determine the C_{sp} (F g^{-1}), E_d (W h kg^{-1}), and P_d (W kg^{-1}).[68]

$$C_{sp} = \frac{I_d t_d}{m(v_2 - v_1)} \qquad (11)$$

$$E_d = \frac{C_{sp} \Delta V^2}{7.2} \qquad (12)$$

$$P_d = \frac{E \times 3600}{t_d} \qquad (13)$$

Here I_d represents the discharge current, t_d represents the discharge duration, m represents the mass put on nickel foil, and ΔV is the applied potential window. The calculated capacitance from GCD for pure WS_2 at current density 0.8 A g^{-1}, 1 A g^{-1}, 1.2 A g^{-1}, 1.4 A g^{-1}, 1.6 A g^{-1}, 1.8 A g^{-1}, and at 2 A g^{-1} are 89.52 F g^{-1}, 85.71 F g^{-1}, 88.57 F g^{-1}, 93.33 F g^{-1}, 99.04 F g^{-1}, 107.14 F g^{-1}, and 104.76 F g^{-1} respectively. Similarly for Fe-WS_2 the specific capacitance at current density 0.8 A g^{-1}, 1 A g^{-1}, 1.2 A g^{-1}, 1.4 A g^{-1}, 1.6 A g^{-1}, 1.8 A g^{-1}, and at 2 A g^{-1} are 97.14 F g^{-1}, 97.61 F g^{-1}, 97.14 F g^{-1}, 93.33 F g^{-1}, 114.28 F g^{-1}, 115.71 F g^{-1}, and 114.28 F g^{-1} respectively (Fig. 9(c)). Fe doping expands the WS_2 lattice, increasing surface area and creating more active sites for charge storage.[69] This expansion improves ion diffusion by allowing easier ion movement. Enhanced electronic conductivity from Fe reduces internal resistance and facilitates efficient charge transfer.[70] These physical changes collectively lead to a higher specific capacitance. The calculated energy density from GCD for pure WS_2 at different current densities is
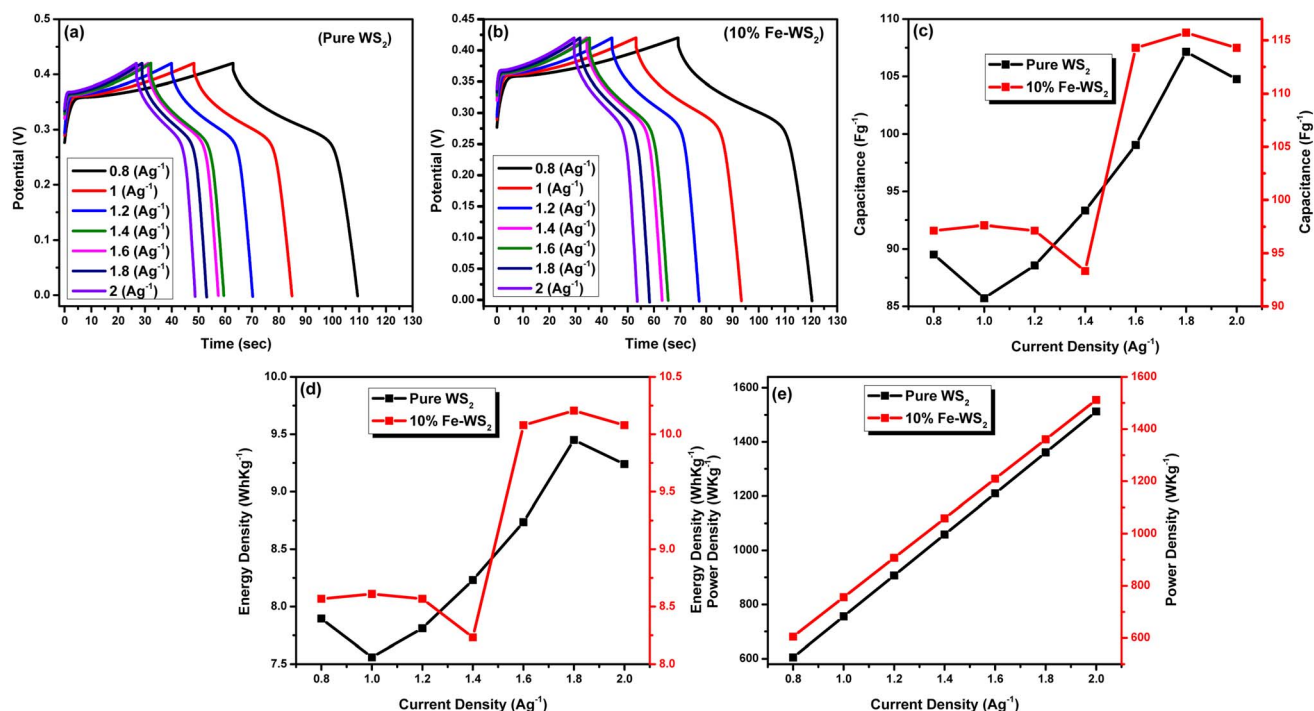
Fig. 9 (a) GCD curves of Pure WS$_2$ (b) GCD curves of Fe-WS$_2$ (c) capacitance of pure and Fe-doped sample (d) energy density of pure and Fe-doped sample (e) power density of pure and Fe-WS$_2$ sample.

0.8 A g^{-1} (7.89 W h kg^{-1}), 1 A g^{-1} (7.56 W h kg^{-1}), 1.2 A g^{-1} (7.81 W h kg^{-1}), 1.4 A g^{-1} (8.23 W h kg^{-1}), 1.6 A g^{-1} (8.74 W h kg^{-1}), 1.8 A g^{-1} (9.45 W h kg^{-1}), and 2 A g^{-1} (9.24 W h kg^{-1}) respectively. Similarly the energy density for Fe-WS$_2$ at different current densities is 0.8 A g^{-1} (8.57 W h kg^{-1}), 1 A g^{-1} (8.61 W h kg^{-1}), 1.2 A g^{-1} (8.57 W h kg^{-1}), 1.4 A g^{-1} (8.23 W h kg^{-1}), 1.6 A g^{-1} (10.08 W h kg^{-1}), 1.8 A g^{-1} (10.21 W h kg^{-1}), and 2 A g^{-1} (10.08 W h kg^{-1}) respectively, (Fig. 9(d)). Fe atoms expand the lattice, creating more space for ions and increasing storage capacity. This lattice expansion improves ion intercalation by allowing ions to enter and exit more easily.[71] Enhanced electronic conductivity from Fe doping reduces resistance, facilitating more efficient charge transfer.[72] These physical changes collectively enable higher energy storage and delivery, resulting in increased energy density. The calculated power density from GCD for pure WS$_2$ at different current density rate is 0.8 A g^{-1} (604.8 W kg^{-1}), 1 A g^{-1} (756 W kg^{-1}), 1.2 A g^{-1} (907.2 W kg^{-1}), 1.4 A g^{-1}(1058.4 W kg^{-1}), 1.6 A g^{-1}(1209.6 W kg^{-1}), 1.8 A g^{-1}(1360.8 W kg^{-1}), and 2 A g^{-1} (1512 W kg^{-1}) respectively in (Fig. 8(e)). The power density for Fe-WS$_2$ at different current density rate is 0.8 A g^{-1} (604.8 W kg^{-1}), 1 A g^{-1} (756 W kg^{-1}), 1.2 A g^{-1} (907.2 W kg^{-1}), 1.4 A g^{-1}(1058.4 W kg^{-1}), 1.6 A g^{-1}(1209.6 W kg^{-1}), 1.8 A g^{-1}(1360.8 W kg^{-1}), and 2 A g^{-1} (1512 W kg^{-1}) (Fig. 9(e)). Fe doping enhances the energy density and capacitance of WS$_2$ by improving ion intercalation and electrochemical activity, but the power density remains unchanged due to similar charge and discharge rates in both pure WS$_2$ and Fe-WS$_2$. This indicates that while Fe doping improves energy storage capacity, the rate at which energy can be delivered remains consistent.[72,73]

The Nyquist plots of the pure WS$_2$ and Fe-WS$_2$ are displayed in Fig. 10(a) and (b). Fig. 10(c) displays both samples Nyquist plots after GCD. The Nyquist plot displays an inclined line at the lower frequency region, which is associated with the Warburg diffusion impedance (W_o).[14] The semicircle at the higher frequency region suggests the solution resistance (R_s) at the first intercept point, and the remaining value of the x-intercept at the second point indicates the charge transfer resistance (R_{ct}).[14] In the higher frequency range, the arc diameters of both electrodes were smaller, which is comparable to the characteristics of combining the pseudocapacitive and usually rapid kinetic diffusion processes. A narrower arc can be seen in the higher frequency area of the Fe-doped Nyquist plot. Table 2 shows the computed decreased values of R_s and R_{ct} for Fe-doped electrode as compared to the pure sample. The higher conductivity brought about by the addition of Fe ions, the greater the disorder, or the decreased contact resistance between the electrode material and Ni foam might all be responsible for this outcome.[14] The ion diffusion coefficients from EIS are calculated by the following relation given below:[74]

$$D_{K^+} = \frac{R^2 T^2}{2A^2 n^4 F^4 C^2 \sigma_w^2} \tag{14}$$

The symbols A, F, n, R, T, and C represent specific quantities: A denotes the electrode area, F stands for Faraday's constant, which is equal to 96 500 C mol^{-1}, n represents the number of reactive electrons per chemical formula, R denotes the gas constant, which has a value of 8.314 J mol^{-1} K^{-1}, T represents the testing temperature, which is measured at 300 K, and C
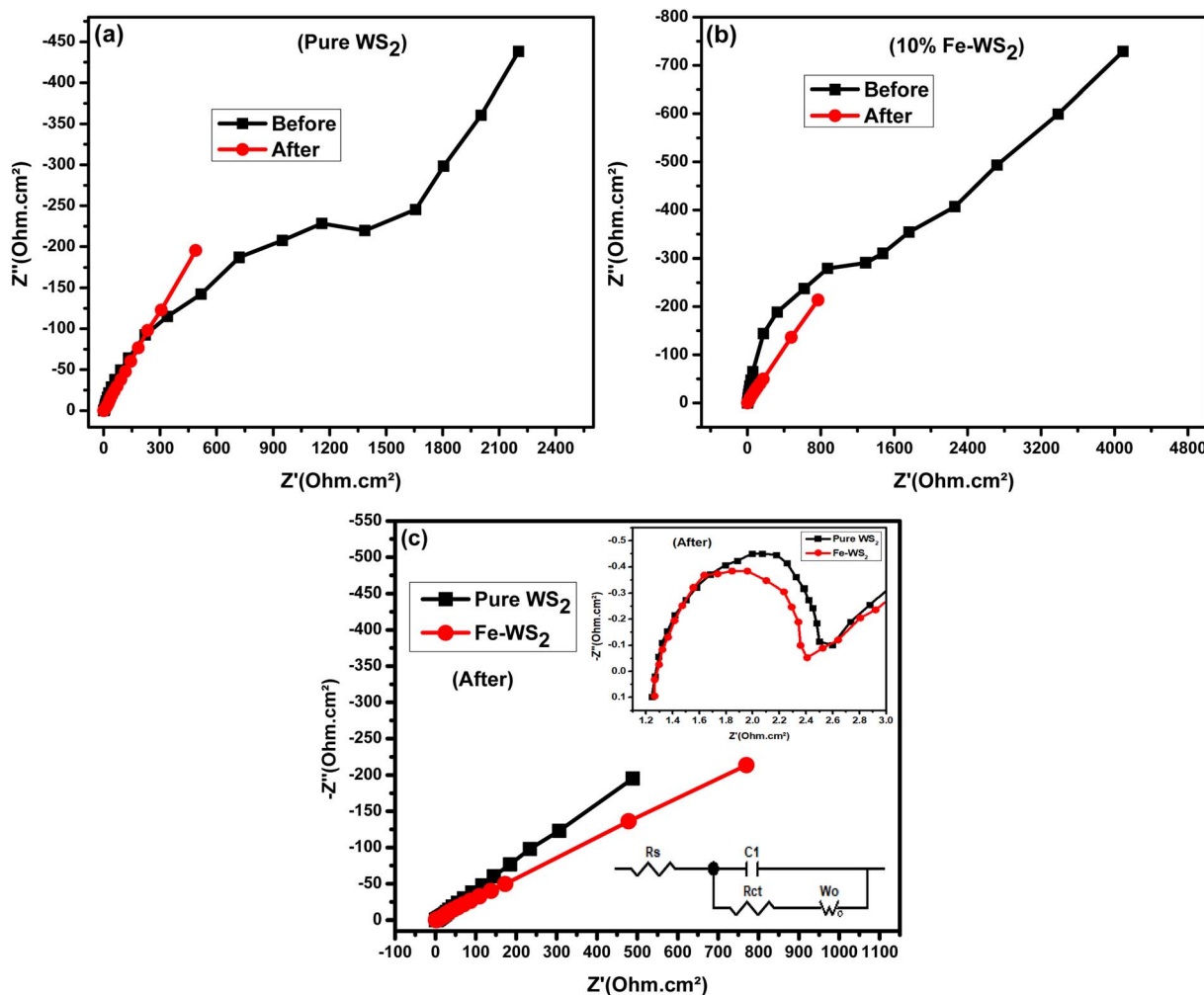
Fig. 10 (a) Nyquist plots before and after of pure WS_2, (b) Nyquist plots before and after of Fe-WS_2 (c) Nyquist plots after GCD of pure and Fe-WS_2.

Table 2 The Calculations of resistance and ion diffusion coefficient from EIS measurements for WS_2 and Fe-WS_2

Samples	Label cycling	R_s (ohm)	R_{ct} (ohm)	D_{K^+} (cm² s⁻¹)
WS_2	Before	1.17	1.40	8.54×10^{-11}
	After	1.24	1.26	8.47×10^{-11}
Fe-WS_2	Before	1.15	1.36	4.41×10^{-10}
	After	1.25	1.19	2.11×10^{-10}

represents the molar concentration of K^+ ions, which is The linear slope, σ_w represents the connection between the frequency and the real component of impedance. The calculated value of ion diffusion coefficient (before) for pure WS_2 is 8.54×10^{-11} and for Fe-WS_2 4.41×10^{-10}, similarly (after) for pure WS_2 is 8.47×10^{-11} and for Fe-WS_2 is 2.11×10^{-10}. After Fe doping in WS_2, ion diffusion increases due to the enhanced d-spacing, which provides more space for ion movement. Due to enhanced d-spacing the process of electrolyte ion intercalation\de-intercalation enhanced. Increased ion diffusion due to Fe doping in WS_2 enhances the charge–discharge

efficiency and capacitance of supercapacitors, leading to improved energy and power density. Moreover, it has been noted that the synthesized Fe-WS_2 electrochemical performance is positively impacted by the presence of impurities such FeS. Improved conductivity is shown by the EIS findings, which show a reduction in R_{ct}. This improvement could result from FeS-facilitated conductive route creation, which improves ion diffusion and charge transfer.[75] Moreover, adding FeS could change the WS_2 electrode electronic structure, which might improve energy storage capacity and raise the density of states at the Fermi level. These structural alterations highlight the intricate relationship between impurity phases and Fe-WS_2 overall electrochemical characteristics.[72]

4. Conclusions

The Fe-doped WS_2 nanoparticles synthesized through an eco-friendly green synthesis method demonstrate significantly enhanced electrochemical properties, making them highly promising for supercapacitors applications. The structural analysis formation of hexagonal structure and enlarge interlayer

spacing. FTIR confirmed the presence of essential W–S, and S–S bonds. The BET analysis confirmed the increased surface area and pore radius as a result of enhanced ions diffusion. The morphology study through Scanning Electron Microscope (SEM) revealed that enhanced porosity of $Fe-WS_2$, as evidenced by the more granular and disordered structure. Methyl blue (MB) dyed adsorption spectra showed that the $Fe-WS_2$ is porous, and as a result, more electrolyte adsorb within the electrode. Electrochemical tests such as CV, GCD, and EIS showed greater cycling stability, which is critical for long-term supercapacitor performance. These findings highlight the potential of Fe-doped WS_2 as an advanced electrode material in energy storage technologies.

Data availability

The data supporting the findings of the article available from the corresponding author, Ali Mujtaba, upon reasonable request.

Conflicts of interest

The authors show that they have no conflict of interest.

Acknowledgements

References

1 L. Phor, A. Kumar and S. Chahal, Electrode materials for supercapacitors: a comprehensive review of advancements and performance, *J. Energy Storage*, 2024, **84**, 110698.

2 B. Ramulu, *et al.*, Improved rate capability and energy density of high-mass hybrid supercapacitor realized through long-term cycling stability testing and selective electrode design, *Mater. Sci. Eng. R Rep.*, 2024, **160**, 100820.

3 Y. A. Kumar, *et al.*, Shaping the future of energy: the rise of supercapacitors progress in the last five years, *J. Energy Storage*, 2024, **98**, 113040.

4 D. Gupta, *et al.*, Metal-Based Nanolubricants: Current and Future Perspectives, *Nanolubricants: Generation and Applications*, 2024, p. 89–133.

5 M. Mirzaei and M. B. Gholivand, Ni and P co-doped WS_2 nanosheets decorated on MWCNTs as an efficient counter electrode for dye-sensitized solar cells, *J. Alloys Compd.*, 2024, **980**, 173535.

6 S. S. Magdum, S. Thangarasu and T. H. Oh, Three-dimensional ternary rGO/VS2/WS2 composite hydrogel for supercapacitor applications, *Inorganics*, 2022, **10**(12), 229.

7 N. Iqbal, *et al.*, Structure Engineering of WS2@Carbon Nanofibers for CO2 Capture, Supercapacitors, and Na-Ion Storage, *ACS Appl. Nano Mater.*, 2024, **7**(11), 12273–12279.

8 V. V. Mohan and R. Rakhi, WS2/Conducting polymer nanocomposite-based flexible and binder-free electrodes for high-performance supercapacitors, *Electrochim. Acta*, 2024, **498**, 144657.

9 K. Kumar and R. Kundu, Doping Engineering in Electrode Material for Boosting the Performance of Sodium Ion Batteries, *ACS Appl. Mater. Interfaces*, 2024, **16**(29), 37346–37362.

10 G. Maduraiveeran, M. Sasidharan and W. Jin, Earth-abundant transition metal and metal oxide nanomaterials: synthesis and electrochemical applications, *Prog. Mater. Sci.*, 2019, **106**, 100574.

11 K. Pandey and H. K. Jeong, Nickel-Doped Tungsten Disulfide for Energy Storage Applications, *J. Nepal Phys. Soc.*, 2023, **9**(3), 7–11.

12 V. V. Mohan, M. Mohan and R. Rakhi, High performance supercapacitors based on WS2 nanoflower electrodes with commercial-level mass-loading, *Surface. Interfac.*, 2023, **42**, 103496.

13 P. Siva and K. Vasu, Enhanced hydrogen evolution and symmetric supercapacitor performance of a Ru-doped multiphase WS2 electrode, *J. Mater. Chem. A*, 2024, **12**(2), 961–967.

14 M. B. Poudel, G. P. Ojha and H. J. Kim, Manganese-doped tungsten disulfide microcones as binder-free electrode for high performance asymmetric supercapacitor, *J. Energy Storage*, 2022, **47**, 103674.

15 C. Poornimadevi, *et al.*, Ab initio study of electronic properties on WS2 monolayer and transition metal doped WS2, *ECS J. Solid State Sci. Technol.*, 2022, **11**(7), 073003.

16 K. Kang, *et al.*, The effects of substitutional Fe-doping on magnetism in MoS2 and WS2 monolayers, *Nanotechnology*, 2020, **32**(9), 095708.

17 G. A. Tigwere, *et al.*, Transition metal (Ni, Cu and Fe) doped MnS nanostructures: effect of doping on supercapacitance and water splitting, *Mater. Sci. Semicond. Process.*, 2023, **158**, 107365.

18 F. U. Haider, *et al.*, Harnessing plant extracts for eco-friendly synthesis of iron nanoparticle (Fe-NPs): characterization and their potential applications for ameliorating environmental pollutants, *Ecotoxicol. Environ. Saf.*, 2024, **281**, 116620.

19 H. Khan, M. Kataria, and M. A. Khan, Antimicrobial Efficacy of Neem Extract–Stabilized Metal Nanoparticles, in *Nanotechnological Approaches in Food Microbiology*, CRC Press, 2020, pp. 55–85.

20 G. Kale, *et al.*, Green synthesis of silver nanoparticles using Azadirachta indica leaves extract and characterization by UV, *Sustain. Dev.*, 2022, **1695**, 1995–1699.

21 M. Alaei, A. M. Rashidi and A. Mahjoub, Two suitable methods for the preparation of inorganic fullerene-like (IF) WS2 nanoparticles, *Iran. J. Chem. Chem. Eng.*, 2009, **28**(2), 91–98.

22 X. Zhang, et al., Preparation and tribological properties of WS2 hexagonal nanoplates and nanoflowers, Nanomaterials, 2019, 9(6), 840.

23 D. Li, et al., Formation of multi-shelled nickel-based sulfide hollow spheres for rechargeable alkaline batteries, Inorg. Chem. Front., 2018, 5(3), 535–540.

24 Z. Wang, et al., Preparation and electrochemical properties of electrospun FeS/carbon nanofiber composites, Ionics, 2020, 26, 3051–3060.

25 M. A. Dar, et al., Electrochemical performance of Fe-doped SnSe material electrodes for supercapacitors, J. Energy Storage, 2024, 94, 112403.

26 R. Sahebi, M. R. Roknabadi and M. Behdani, Semi-transparent Schottky junction solar cell based on evaporated CdSe thin films: influence of post-deposition air-annealing, Optik, 2020, 204, 164204.

27 M. Khan, et al., The structural, optical and photovoltaic properties of Zn-doped MAPbI2 Br perovskite solar cells, Phys. Chem. Chem. Phys., 2024, 26(15), 12210–12218.

28 M. Khan, et al., The structural, optical and photovoltaic properties of Zn-doped MAPbI2 Br perovskite solar cells, Phys. Chem. Chem. Phys., 2024, 26(15), 12210–12218.

29 C. Li, et al., Recent Excellent Optoelectronic Applications Based on Two-Dimensional WS2 Nanomaterials: A Review, Molecules, 2024, 29(14), 3341.

30 M. Khan, et al., Enhanced efficiency of CsPbIBr2 perovskite solar cells through dual-layer ETL engineering, J. Sol-Gel Sci. Technol., 2024, 111(3), 754–765.

31 M. Jiang, et al., The coupled effects of grain boundary strengthening and Orowan strengthening examined by dislocation dynamics simulations, Comput. Mater. Sci., 2024, 231, 112602.

32 A. Jain and A. Varshney, Effect of grain size and dislocation density on the work hardening behavior of SS 304, J. Mater. Eng. Perform., 2024, 1–18.

33 M. Khan, et al., Impact of Ce doping on the optoelectronic and structural properties of a CsPbIBr 2 perovskite solar cell, Phys. Chem. Chem. Phys., 2024, 26(5), 4166–4173.

34 A. Karamat, et al., Revolutionizing photocatalysis: synergistic enhancement of structural, optical, and photodegradation properties in Be-doped V2O5 nanoparticles for efficient methylene blue removal, Results Chem., 2024, 101600.

35 M. Zhang, et al., Theoretical study of mechanical and thermodynamic properties of W–Fe alloys: promising ultra-high temperature alloy materials, Vacuum, 2024, 222, 113047.

36 M. Arslan, et al., Investigating the influence of cerium doping on the structural, optical and electrical properties of ZnNiMgFe2-xCexO4 soft ferrites, J. Mol. Struct., 2024, 1318, 139237.

37 A. Kumar and M. Shah, Examining the effects of crystalline flaws on the electrochemical performance of different (Fe, Co) co-doped nickel oxide nanostructures in supercapacitors, J. Energy Storage, 2024, 92, 112188.

38 H. Shalom, et al., Chemical control of the surface of WS2 nanoparticles, Chem. Phys. Lett., 2020, 761, 138052.

39 A. Kumar, M. Sharma and R. Vaish, WS2 nanoparticles screen printed cotton for dual piezo-and photocatalytic antibacterial and dye degradation performance, Ind. Crops Prod., 2024, 209, 117954.

40 P. Phogat, R. Jha and S. Singh, Carbon nanospheres-induced enhanced capacitive dynamics in C/WS2/WO3 nanocomposites for high-performance electrochemical capacitors, Mater. Sci. Eng. B, 2024, 304, 117390.

41 M. Khan, et al., Enhancing the structural and optoelectronic properties of double ETL nickel-doped CsPbIBr2 perovskite solar cells, CrystEngComm, 2024, 26, 3535–3546.

42 H. Li, et al., Enhanced removal of Sb (III) and Sb (V) using biosynthesized iron sulfide nanoparticles: identification of biomolecules in the capping layer and its functions, Appl. Surf. Sci., 2023, 628, 157372.

43 Z. Wu, et al., Removal of As (V) by iron-based nanoparticles synthesized via the complexation of biomolecules in green tea extracts and an iron salt, Sci. Total Environ., 2021, 764, 142883.

44 S. Shahabuddin, et al., Synthesis and characterization of 2D-WS2 incorporated polyaniline nanocomposites as photo catalyst for methylene blue degradation, Nanomaterials, 2022, 12(12), 2090.

45 R. Huirache-Acuña, et al., Synthesis and characterization of WO3 and WS2 hexagonal phase nanostructures and catalytic test in sulfur remotion, J. Mater. Sci., 2009, 44, 4360–4369.

46 Z. Lu, et al., Preparation and tribological properties of WS2 and WS2/TiO2 nanoparticles, Tribol. Int., 2019, 130, 308–316.

47 R. Tyer, et al., Systematic theoretical study of the spin and orbital magnetic moments of 4 d and 5 d interfaces with Fe films, Phys. Rev. B:Condens. Matter Mater. Phys., 2003, 67(10), 104409.

48 G. Ramalingam, et al., Quantum confinement effect of 2D nanomaterials, in Quantum dots-fundamental and applications, IntechOpen, 2020.

49 M. Khan, et al., Impact of molybdenum doping on the optoelectronic and structural properties of CsPbIBr2 perovskite solar cell, Phys. B, 2024, 678, 415758.

50 I. N. Reddy, et al., Effect of ball milling on optical properties and visible photocatalytic activity of Fe doped ZnO nanoparticles, Mater. Sci. Eng. B, 2019, 240, 33–40.

51 M. Khan, et al., Impact of Cr doping on the structural and optoelectronic properties of a CsPbIBr 2 perovskite solar cell, New J. Chem., 2024, 48(16), 7205–7212.

52 J. L. Lyons, D. Wickramaratne and A. Janotti, Dopants and defects in ultra-wide bandgap semiconductors, Curr. Opin. Solid State Mater. Sci., 2024, 30, 101148.

53 A. Z. Muaawia, et al., Enhanced medicinal applications of Co-doped Zn0.5Ni0.5Fe2-xO4 for (X= 0.00 and 0.0250) soft ferrites: a structural analysis, J. Appl. Math., 2023, 1(2), 237.

54 M. Khan, et al., Bandgap reduction and efficiency enhancement in Cs2AgBiBr6 double perovskite solar cells through gallium substitution, RSC Adv., 2024, 14(8), 5440–5448.

55 S. Pandey, et al., Systematic Investigation of Structural, Morphological and Optical Properties of Fe Doped ZnO

Nanorods and Its Nanocomposite with Graphite Oxide, *J. Mater. Eng. Perform.*, 2024, 1–20.

56 C. Gong, *et al.*, Utilizing Se vacancies as electronic traps to synergize impedance matching and dipole polarization with ultrathin strategy to boost Fe-Se electromagnetic wave absorption, *Chem. Eng. J.*, 2024, **480**, 147793.

57 Z. Sun, *et al.*, The structural and optical properties of Mn/Fe-doped KDP crystals: a first-principles calculation, *J. Electron. Mater.*, 2024, **53**(2), 891–898.

58 M. Khan, *et al.*, 700 keV Au ions beam effect on the structural, optical and photovoltaic properties of MAPbI3 solar cells, *Ceram. Int.*, 2023, **49**(5), 8546–8553.

59 H. Zhao, *et al.*, Adsorption and Sensing Behavior of Cr-Doped WS2 Monolayer for Hazardous Gases in Agricultural Greenhouses: A DFT Study, *Mater. Today Commun.*, 2024, 109405.

60 B. Pant, *et al.*, Hydrothermally synthesized ZnO/WS2 composite with impressive photocatalytic, antibacterial, and electrochemical performances, *Inorg. Chem. Commun.*, 2024, 112630.

61 Y. Liu, *et al.*, Ni/WS2/WC Composite Nanosheets as an Efficient Catalyst for Photoelectrochemical Hydrogen Peroxide Sensing and Hydrogen Evolution, *Materials*, 2024, **17**(5), 1037.

62 H. M. Danamah, *et al.*, Surface morphology-tailored electrochemical supercapacitor and better hydrogen evolution reaction activities of Bi2S3 nanostructures, *J. Energy Storage*, 2024, **97**, 112323.

63 C. R. Babu, *et al.*, Symmetric supercapacitor based on Co3O4 nanoparticles with an improved specific capacitance and energy density, *J. Energy Storage*, 2024, **80**, 110382.

64 F. Faisal, *et al.*, Facile fabrication of Mn doped WSe2 as an electrode material for supercapacitor application, *Electrochim. Acta*, 2024, 144876.

65 K. K. Das, *et al.*, Improving Charge Carrier Separation through S-Scheme-Based 2D–2D WS2/Sulfur-Doped g-C3N4 Heterojunctions for a Superior Photocatalytic O2

Reduction Reaction, *ACS Appl. Energy Mater.*, 2024, **7**(15), 6360–6375.

66 L.-Y. Xie and J.-M. Zhang, Electronic structures and magnetic properties of the transition-metal atoms (Mn, Fe, Co and Ni) doped WS2: a first-principles study, *Superlattices Microstruct.*, 2016, **98**, 148–157.

67 M. G. Bianchi, *et al.*, Engineering the electrical and optical properties of WS2 monolayers via defect control, *Adv. Sci.*, 2024, **11**(4), 2305162.

68 A. Mujtaba, *et al.*, Optical, Structural, and Electrical Performance of CsPbIBr2 Perovskites with Zirconium Doping and Bilayer ETLs, *J. Solid State Chem.*, 2024, 124827.

69 D. Cao, *et al.*, Fe13+-ion irradiated WS2 with multi-vacancies and Fe dopants for hydrogen evolution reaction, *FlatChem*, 2021, **27**, 100247.

70 F. Guo, *et al.*, Enhanced Charge Transfer via Heterogeneous Doping Promotes Hematite Photoelectrodes for Efficient Solar H2O2 Synthesis, *ACS Catal.*, 2024, **14**(7), 4369–4378.

71 A. Mujtaba, *et al.*, Tailoring the structural, optical, photoluminescence, dielectric and electrical properties of Zn0.6Ni0.2Mg0.2Fe2-xLaxO4 (x= 0.00, 0.0125, 0.0250, 0.0375), *J. Mater. Res. Technol.*, 2023, **23**, 4538–4550.

72 Z. Yu, *et al.*, Combining bulk charge transport and surface charge transfer to design titanium-doped hematite homojunction photoanodes, *J. Phys. Chem. C*, 2022, **126**(9), 4296–4305.

73 B. S. Almutairi, *et al.*, Impact of La doping on the optoelectronic and structural properties of CsPbIBr2 perovskite solar cell, *Opt. Mater.*, 2024, **152**, 115415.

74 X. Luo, *et al.*, Constructing multi-dimensional migration channel by nickel-doped WS2 composite: high speed sodium and potassium ion storage kinetics in WS2 nanosheets, *Chem. Eng. J.*, 2023, **464**, 142579.

75 D. T. Pham, *et al.*, Facile synthesis of pyrite (FeS2/C) nanoparticles as an electrode material for non-aqueous hybrid electrochemical capacitors, *Nanoscale*, 2018, **10**(13), 5938–5949.